Materials & Design 207 (2021) 109857

Contents lists available at ScienceDirect

Materials & Design

journal homepage: www.elsevier.com/locate/matdes

High-fidelity modelling of selective laser melting copper alloy: Laser reflection behavior and thermal-fluid dynamics

Zhihao Ren [a,b], David Z. Zhang [a,b,c,*], Guang Fu [d,*], Junjie Jiang [e], Miao Zhao [a,b]

[a] State Key Laboratory of Mechanical Transmissions, Chongqing University, Chongqing 400044, China
[b] Chongqing Key Laboratory of Metal Additive Manufacturing (3D Printing), Chongqing University, Chongqing 400044, China
[c] College of Engineering, Mathematics and Physical Sciences, University of Exeter, North Park Road, Exeter EX4 4QF, UK
[d] School of Mechanical Engineering, Guizhou University, Guiyang 550025, Guizhou Province, China
[e] Mechanical and Electrical Engineering College, Zhengzhou University of Light Industry, Zhengzhou 450002, China

HIGHLIGHTS

- A high-fidelity CFD model that predicts the SLM process of Cu-Cr-Zr alloy.
- Implementation of ray-tracing method coupled with temperature-dependent absorption.
- In-situ laser absorptivity measurements.
- Good consistency between simulations and experiments.
- Underlying mechanisms of laser reflection.

GRAPHICAL ABSTRACT

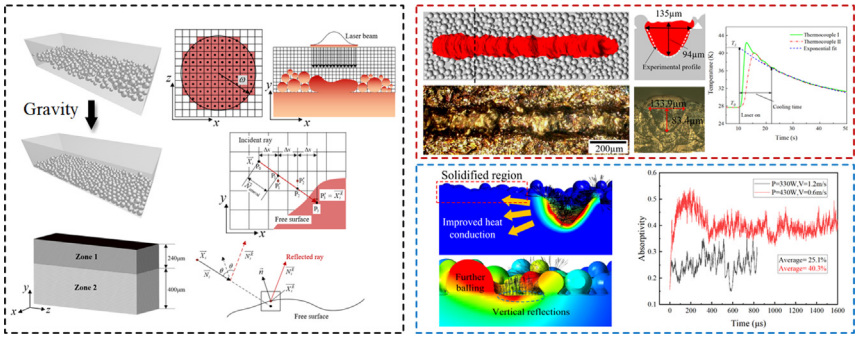

ARTICLE INFO

Article history:
Received 25 February 2021
Revised 21 May 2021
Accepted 29 May 2021
Available online 1 June 2021

Keywords:
Selective laser melting
Ray-tracing method
Temperature-dependent absorption
Laser reflection
Copper

ABSTRACT

Despite of the promising capabilities of selective laser melting (SLM), the poor formability of copper and its alloys is a critical challenge for industrial applications, which is widely-believed attributed to the high reflectivity of copper. Due to the difficulty of observing laser reflections, current understanding on the laser reflection mechanisms is still vague and unclear. This work constructs a high-fidelity CFD model coupled with a ray-tracing method to visualize the flow kinetics and reflection behavior during SLM Cu-Cr-Zr alloy. Considering the material specificity of copper, a temperature-dependent absorption rule is introduced to overcome the simulation deviation caused by the widely-used Fresnel absorption, showing good agreement with experiments in terms of track width and depth. The in-situ absorptivity measurement experiments are further conducted to compare with simulations with the error less than 2%. Additionally, different reflection mechanisms for continuous and distorted tracks are revealed. At relatively high linear energy density (LED), the global absorptivity undergoes a rise and a decrease in the initial stage, and finally gets stable. At low LED level, the surface tension drives the melt pool to form isolated balls and exposed plat surface, which is responsible for the intense absorptivity oscillation as the balling effect occurs.

1. Introduction

Selective laser melting (SLM) as a branch of metal additive manufacturing (MAM), is a disruptive technology that brings the

* Corresponding authors at: State Key Laboratory of Mechanical Transmissions, Chongqing University, Chongqing 400044, China (D.Z. Zhang).
E-mail addresses: zhangzw@cqu.edu.cn (D.Z. Zhang), gfu@cqu.edu.cn (G. Fu).

https://doi.org/10.1016/j.matdes.2021.109857
0264-1275/

manufacturing industry huge possibilities. In the SLM process, a thin layer of metal powders is selectively irradiated by a fast-scanning laser beam. As the powders reach the melting point, the powders are coalesced to form the melt-pool that undergoes rapid cooling and solidifies after the laser beam moves away. With multiple melting and solidification, a dense entity can gradually be built in three-dimensions in a layer-by-layer way [1]. The layer-by-layer approach offers various advantages over conventional manufacturing processes in terms of design flexibility, effective material usage, short lead time and multifunctional integration [2].

With these advantages, use of SLM is growing rapidly in relevant sectors, including medical, automobile, aerospace and defense industries, thus accompanied with its material palette increasingly extended. Especially, copper as well as its alloys has attracted significant interest in SLM academia and society, due to the superior electrical and thermal conductivity of copper which holds broad potentials in the production of electronic devices, thermal management systems and aerospace engine structures. With these advantages, numerous researches [3–5] on the feasibility of copper and its alloys by SLM have been carried out and even several practical applications [6,7] have been reported.

However, one critical challenge proposed by many researches is that copper as well as its alloys is more susceptible to defects (e.g. porosity, cracking, poor density, etc.) owing to insufficient energy input caused by its extremely high reflectivity in a 1.06 μm laser [8]. To overcome this challenge, considerable efforts on experiments have primarily focused on acquiring higher energy input. For example, in a SLM system commonly equipped with a Nd: YAG or YLF laser, this problem can be alleviated by updating laser devices with higher power from the initial 200 W [9], to 400 W [4,10,11], then to 1 kW [8] and even 1.8 kW [3]. Alternative way is to increase the laser absorptivity of copper by using green light (wave length = 515 nm) which possesses 40% absorptance in comparison to 5% for the near-infrared light (wave length = 1064/1070 nm) at room temperature [12]. Although these experimental advances have obtained dense SLMed parts of copper and its alloy by increasing the laser power or frequency, the underlying forming mechanisms responsible for the poor formability are still unclear and vague. The physical properties of materials (including the viscosity, surface tension, etc.) undoubtedly have influence on the melt flow behaviors during SLM. Tang et al. [13] suggest that the high surface tension and viscosity can suppress the humping phenomenon and lead to smoother surface morphology. This change can be obvious only when the values of these parameters vary in multiples. However, there is not too much difference in both the viscosity and surface tension between copper and other commonly SLM-used materials (Ti6Al4V and 316L stainless steel). Generally, it is believed that the high reflectivity of copper makes it difficult to form a sufficient and stable melt pool during SLM, but how the reflection behavior happens and how it matters during manufacturing are left to be revealed. Since SLM is characterized as a highly transient and complex process with multiple physical phenomena (e.g. laser-powder interaction, material phase transition, capillary action, evaporation, etc.) occurring simultaneously in microseconds, it would be either unavailable or quite expensive to have immediate analysis by using in-situ monitoring systems, especially for the data capturing of laser absorptance [14]. Therefore, conducting a high-fidelity numerical simulation is chosen as an alternative to reveal the underlying physics.

Numerical simulation for SLM process is a crucial approach to better understand the complex physical phenomena. For example, a CFD model is usually developed to predict the thermal-fluid dynamics within the melt pool, where the formation mechanisms of original defects (pores [15], denudation [16], spatter [17], balling [18], etc.) in SLM can be revealed. However, there are obvious limitations on how to deal with the laser-material interaction in many CFD researches of SLM. For instance, recent studies [16,18–20] have traced laser-material interaction surface to apply a Gaussian laser heat source, but their models only assume a constant equivalent absorptivity with the multiple laser reflections neglected. Gusarov et al. [21] develop a volumetric heat source with the decay of the energy intensity in a powder layer to consider the laser reflection/absorption behavior. Some studies [15,17,22] use an adaptive volumetric heat source model developed by Xu et al. [23] to consider the multiple laser reflections in the key hole. For the volumetric heat sources, melting happens simultaneously everywhere inside powder particles, leading to unrealistic wetting behavior [16]. Additionally, these volumetric heat source models only consider the laser reflection/absorption in a specific state (i.e., powders [21] or a keyhole [23]), while the laser does not interact with either powder particles or a keyhole during SLM. The absence of considering the dynamic evolution of the melt pool further weakens the authenticity of the laser model. In fact, the laser absorptance is closely related to laser reflection behavior that is affected by the irradiated object (e.g. unfused powders, flat surface, molten liquid or key hole) [24]. For instance, Boley et al. [25] conduct ray-tracing simulations based on Fresnel absorption to calculate the laser absorption of different materials at room temperature. Their results demonstrate that the overall absorptivity of powders is markedly greater than that of a flat surface due to multiple laser reflections between powders particles. Moreover, Bayat et al. [26] further introduce a ray-tracing method into the CFD model to calculate the laser reflection and absorption during SLM of 316L stainless steel. Their work shows that the overall absorptance will be also enhanced due to multiple laser reflections in a key hole when excessive laser power is applied.

Undoubtedly, the ray-tracing method largely reflects the reality of the laser-material interaction. However, to date, researches [13,14,27,28] that are coupled with the ray-tracing method all use the Fresnel absorption to determine the local absorptivity that only depends on the incidence angle and refractive index of material. Little has considered the influence of temperature evolution. It is worth noting that the absorptivity for most metals will increase with the temperature elevated, and the temperature dependence of laser absorption should be also concerned since heating is the name of the game [12,29–31]. In addition, when a material with high reflectivity (e.g. the calculated absorptivity for a flat plate of copper is only 0.011 at room temperature [25]) is chosen for SLM simulation, the CFD model that only considers the Fresnel absorption may lead to huge deviation, where the metal powders fail to melt down due to insufficient energy input. This will be also discussed in detail in section 4.1. In this point of view, it would be of necessity to further improve the simulation fidelity by a combination of the ray-tracing and the temperature-dependent absorption.

At present work, since copper alloys are more common in practical industrial applications than pure copper, we therefore take the Cu-Cr-Zr alloy as a representative material for this study, which is a high conductivity, high-strength copper alloy for use in high heat flux applications such as rocket engine combustion [32]. To have unique insights into the laser reflection behavior in SLM Cu-Cr-Zr alloy, a ray-tracing algorithm that calculates the multiple laser reflections is coupled into a CFD model, so that the variation of laser reflections with the melt pool evolution can be predicted and visualized. A comparison of absorption rule between the Fresnel and a temperature-dependent rule has been conducted, which shows that the latter is more in line with the experimental results in terms of track width and depth. The in-situ absorptivity measurement experiments are also carried out to further validate the accuracy of this model with the error between experimental and simulated results lower than 2%. Furthermore, a continuous

single-track as well as the balling effect has been simulated with different LED levels applied. For both cases, the different mechanisms of laser reflection are revealed, and the corresponding variation of global absorptivity is characterized.

2. Simulation methods and experiment

During SLM process, an intensive energy flux is deposited on a small area of metal surface, which can easily melt down and even further evaporate the metal powders. To simulate this complex process, multiple phenomena should be considered, e.g., thermo-capillary forces, recoil pressure, and the laser-powder interaction. Therefore, in this work, a high-fidelity simulation framework is established to predict the temperature field and material's flow behavior during processing, including 1) a DEM (discrete element method) model to initialize a powder bed packing configuration, and 2) a CFD (computational fluid dynamics) model to predict the melting process. Details of these models are discussed as follows.

2.1. Powder bed configuration by DEM

DEM is a well-established numerical technique, which allows modelling of discrete granular materials behaviors following a given force-displacement relation [33]. The translation and rotation of each powder particle is determined by Newton's second law. In this work, a commercial DEM software EDEM is used to model the random packing of copper particles laid on the substrate. The Hertz-Mindlin (No slip) model is adopted to describe the contact force between particles with the schematic diagram shown in Fig. 1. In this model, the normal force component is based on Hertzian contact theory, and the tangential force is based on Mindlin-Deresiewicz work. Both normal and tangential forces have damping components where the damping coefficient is related to the coefficient of restitution. The tangential friction force follows the Coulomb law of friction model. The rolling friction is implemented as the contact independent directional constant torque model. All contact forces can be determined as follows [34]:

$$F_n = \frac{4}{3}E^*\sqrt{R^*}\delta_n^{\frac{3}{2}} \tag{1}$$

$$F_n^d = -2\sqrt{\frac{5}{6}}\beta\sqrt{S_n m^*}\,v_n^{\overrightarrow{rel}} \tag{2}$$

$$F_t = -S_t\delta_t \tag{3}$$

$$F_t^d = -2\sqrt{\frac{5}{6}}\beta\sqrt{S_t m^*}\,v_t^{\overrightarrow{rel}} \tag{4}$$

$$\tau_i = -\mu_r F_n R_i \omega_i \tag{5}$$

where F_n and F_t are the forces in normal and tangential direction respectively, F_n^d and F_t^d are the damping forces in both directions, and τ_i stands for the torque applied to the contacting surfaces. The coefficients used in Eqs. (1)–(5) can be accounted for as follows:

E^*, R^*, m^* are the equivalent Young's modulus, equivalent radius and equivalent mass respectively. δ_n and δ_t stand for the normal and tangential overlap. S_n and S_t are defined as the normal stiffness and tangential stiffness. $v_n^{\overrightarrow{rel}}$ and $v_t^{\overrightarrow{rel}}$ are normal and tangential components of the relative velocity. β is a constant related to the coefficient of restitution, μ_r is the coefficient of rolling friction, R_i is the distance of the contact point from the center of mass, and ω_i stands for the unit angular velocity vector of the object at the contact point.

In this work, the realistic powder size distribution is obtained by a laser particle size analyzer (Mastersizer 2000, Malvern Instruments Ltd., Malvern, UK), with particle size distribution shown in Fig. 2. The copper powders are modelled as normally distributed spheres with an average diameter of 32 μm, a standard deviation of 6 μm and diametral cutoffs at 20 and 47 μm. Then, a cloud of powders is generated by EDM and lands on the substrate under gravity as shown in Fig. 3. The layer thickness was set as 54.7 μm and any particles that have the top surface height (center height plus radius) greater than 54.7 μm are removed from the DEM result. The coordinates and radius of DEM powders are subsequently extracted into the CFD model to initialize the domain configuration.

2.2. CFD laser-powder interaction model

2.2.1. Governing physics of melt flow kinetics

In this work, a CFD model is developed based on a commercial CFD software (ANSYS Fluent) to simulate the thermo-fluid dynamics of the powder bed with the irradiation of high-energy laser beam. For sake of simplification, the liquid within molten pool is assumed to be incompressible and Newtonian with laminar flow. As described in most literatures, the motion of melt flow within the molten pool is governed by three basic physical conservation laws, i.e., the conservation of mass, momentum and energy, which are given as follows [19,20,27]:

The mass conservation equation:

$$\frac{\partial\rho}{\partial t} + \nabla\cdot(\rho\vec{v}) = 0 \tag{6}$$

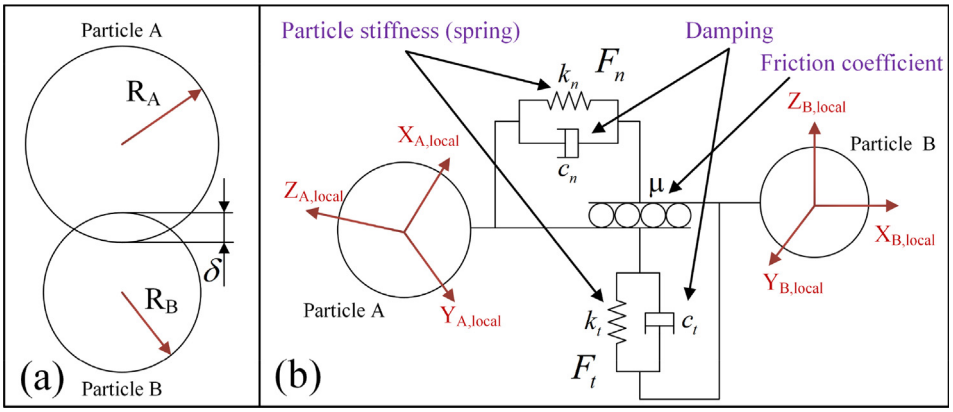

Fig. 1. (a) Contact condition and (b) vibration model of two colliding particles.

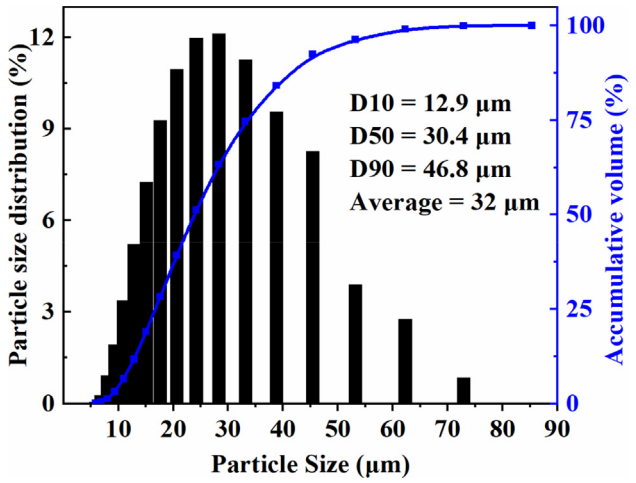

Fig. 2. The size distribution of the Cu-Cr-Zr powders.

The momentum conservation equation:

$$\frac{\partial}{\partial t}(\rho\vec{v}) + \nabla\cdot(\rho\vec{v}\vec{v}) = -\nabla p + \rho\vec{g} + \nabla\cdot\hat{\tau} + \overrightarrow{f_{damp}} + \overrightarrow{f_{st}} + \overrightarrow{f_M} + \overrightarrow{P_{recoil}} \tag{7}$$

The energy conservation equation:

$$\frac{\partial}{\partial t}(\rho h) + \nabla\cdot(\rho\vec{v}h) = \nabla\cdot(k\nabla T) + q_{evp} + q_{CR} + q_{laser} \tag{8}$$

$\vec{v}$ and $\vec{g}$ bid the velocity and gravity acceleration vector, respectively. ρ, μ, k stand for the material properties of density, viscosity and thermal conductivity, respectively. p and T refer to the pressure field and temperature in several. The viscous stress tensor $\hat{\tau}$ is expressed as:

$$\hat{\tau} = \mu[(\nabla\vec{v} + \nabla\vec{v}^T) - \frac{2}{3}\nabla\cdot\vec{v}\hat{I}] \tag{9}$$

where $\hat{I}$ demonstrates the unit tensor matrix.

The free surface of copper phase can be captured with the volume of fluid (VOF) algorithm [35] applied and the volume fraction of copper phase follows the following conservation equation:

$$\varphi_m + \varphi_g = 1 \tag{10}$$

$$\frac{\partial(\rho\varphi_m)}{\partial t} + \nabla\cdot(\rho\varphi_m\vec{v}) = 0 \tag{11}$$

where φ_m stands for volume fraction of metallic phase and the subscript $()_g$ demonstrates the gas phase (the argon). Since a two-phase flow is considered in this work, the mixture material properties is determined by a simple mixing rule: $\xi = \varphi_m\xi_m + \varphi_g\xi_g$, where ξ refers to ρ, μ and k.

To simulate the melting/solidification process during SLM, the widely used enthalpy-porosity method is introduced in this model. A linear function γ is defined dependent on temperature to identify the physical state of metal phase (solid/liquid), which is described as:

$$\gamma = \begin{cases} \gamma = 0 & T < T_s \quad \text{solid} \\ \gamma = \frac{T-T_s}{T_l-T_s} & T_s \leqslant T \leqslant T_l \quad \text{liquid - solid mushy zone} \\ \gamma = 1 & T > T_l \quad \text{liquid} \end{cases} \tag{12}$$

where T_s and T_l are solidus and liquidus temperature of copper, respectively. To describe the release process of latent heat, the specific enthalpy of copper h in Eq. (8) is associated with γ and can be expressed as:

$$h = h_{ref} + \int_{T_{ref}}^{T} C_p dT + \gamma L_m \tag{13}$$

where h_{ref}, C_p, T_{ref} and L_m stand for the reference enthalpy, specific capacity, reference temperature and latent heat of melting. To model the melting/solidification front, a damping force term $\overrightarrow{f_{damp}}$ is added to the momentum equation and defined as:

$$\overrightarrow{f_{damp}} = \frac{(1-\gamma)^2}{(\gamma^3+\varepsilon)}A_{mush}\vec{v} \tag{14}$$

where $A_{mush} = 10^{14}$ [36] is the mushy zone constant and ε is a small constant avoid division by zero.

The right hand side terms $\overrightarrow{f_{st}}$, $\overrightarrow{f_M}$, $\overrightarrow{P_{recoil}}$ in Eq. (7) indicate the surface tension, temperature-dependent Marangoni shear force, and vapor recoil pressure. The surface tension is regarded as the dominant driving force in the melt flow during SLM [37], and is written as:

$$\overrightarrow{f_{st}} = \sigma\kappa\vec{n}|\nabla\varphi_m|\frac{2\rho}{\rho_m+\rho_g} \tag{15}$$

where σ is the surface tension coefficient, κ is the surface curvature of metal free surface, and $\vec{n}$ stands for the unit surface normal vector? As suggested in the literature [38], the term $|\nabla\varphi_m|$ is used to convert the surface forces into smeared volumetric forces in the interface cells. Additionally, a multiplier term $\frac{2\rho}{(\rho_m+\rho_g)}$ is introduced to redistribute the interfacial forces towards the metal phase to avoid high acceleration flow in the gas phase.

The Marangoni shear force is expressed as:

$$\overrightarrow{f_M} = \frac{d\sigma}{dT}\left[\nabla T - \vec{n}(\vec{n}\cdot\nabla T)\right]|\nabla\varphi_m|\frac{2\rho}{\rho_m+\rho_g} \tag{16}$$

where $\frac{d\sigma}{dT}$ is the temperature coefficient of surface tension.

The vapor recoil pressure is expressed as [39]:

$$\overrightarrow{P_{recoil}} = 0.54P_0\exp\left(\Delta L_v\frac{T-T_v}{RTT_v}\right)\vec{n}|\nabla\varphi_m|\frac{2\rho}{\rho_m+\rho_g} \tag{17}$$

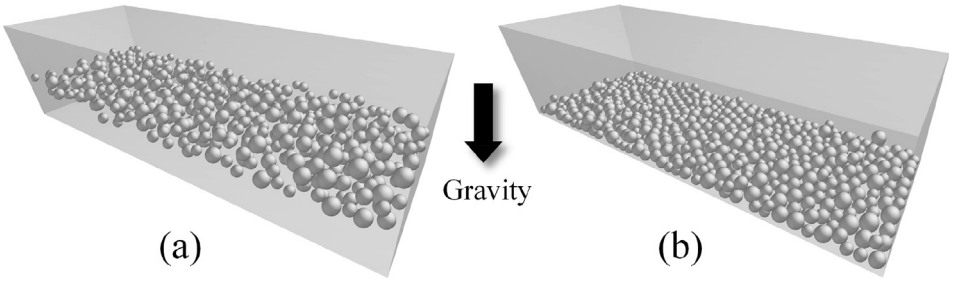

Fig. 3. (a) The falling process of powder particles under gravity, and (b) the powder layer generated by DEM.

where P_0, ΔL_v, T_v and R demonstrate the atmospheric pressure, latent heat of evaporation, boiling temperature and universal gas constant, respectively.

2.2.2. Surface cooling boundary condition

For the energy conservation, the cooling conditions are considered as an essential part to restrict the peak temperature within the molten pool to a reasonable range, including the heat dissipation due to radiation and convection, and the heat loss of evaporation.

The heat loss of evaporation is defined as [39]:

$$q_{evp} = 0.82 \times \frac{\Delta L_v}{\sqrt{2\pi MRT}} P_0 \exp\left(\Delta L_v \frac{T - T_v}{RTT_v}\right) |\nabla \varphi_m| \frac{2\rho C_p}{\rho_m C_{pmetal} + \rho_g C_{pgas}} \tag{18}$$

where M, C_{pmetal}, C_{pgas} denotes the Molar mass of metal, specific heat of metal and specific heat of gas, respectively. Here, using an analogical reason as for the smeared surface forces in Eqs. (15)-(17), one can also use a multiplier term $\frac{2\rho C_p}{(\rho_m C_{pmetal} + \rho_g C_{pgas})}$ to redistribute the heat input towards the region of higher ρC_p, i.e. copper [38].

The heat loss due to radiation and convection is expressed as:

$$q_{CR} = -\left[h_c(T - T_{ab}) + \sigma_s \varepsilon (T^4 - T_{ab}^4\right] |\nabla \varphi_m| \frac{2\rho C_p}{\rho_m C_{pmetal} + \rho_g C_{pgas}} \tag{19}$$

where h_c, σ_s, ε, T_{ab} are the convection coefficient, Stefan-Boltzmann constant, emissivity and ambient temperature, respectively.

2.2.3. Multiple laser reflection model with ray-tracing method

There are several ways to simulate the thermal impact of the laser on the metal material. For simplification of the calculation, most literatures commonly use a moving heat flux, moving surface heat source [19,36], moving volumetric heat source [22,40] or a moving volumetric heat source with the optical penetration depth considered [15,17]. However, these ways do not consider the surface evolution after the powder bed is heated and fused by the laser beam. Thus, they not only weaken the fidelity of the numerical model undoubtedly, but cannot access the reflection behavior of laser rays, which is quite important especially for materials with high reflectivity. In this work, to better model the actual laser-material interaction, a ray-tracing method depended on mesh grids is adopted, which is consisted of three procedures: (1) discretization and initialization of Gaussian laser beam, (2) searching laser-material interaction cells, (3) calculating the reflected rays and cycling.

(1) Discretization and initialization of Gaussian laser beam.

The laser flux emitted from the focusing lens is assumed to follow a planar Gaussian distribution with the following expression:

$$I(x,z) = \frac{2P_{laser}}{\pi\omega^2} \exp\left[-2\frac{(x_0 + v_0 t - x)^2 + (z_0 - z)^2}{\omega^2}\right] \tag{20}$$

where P_{laser}, ω, v_0 stand for the laser power, beam radius and scanning velocity, respectively. $(x_0 + v_0 t,\ z_0)$ denotes the beam center. As presented in Fig. 4(a), the laser beam in the waist section is firstly discretized into bundles of sub-rays with a resolution of $\Delta x = 4$ μm which is equal to the gird size applied to this model. Several variables are declared to define the ray's properties, containing the ray's coordinate X_i, direction vector $\overrightarrow{N_i}$, laser power intensity P^i_{laser} and number of collisions with free surface R_i. The subscript i identify the ray's sequence. The ray's coordinate $X_i = (x_i, y_i, z_i)$ is initialized within the waist section and have the maximum y-direction coordinate in the computational domain. The corresponding initial power intensity of each sub-ray is set as $P^i_{laser} = I(x_i, z_i)$. The $\overrightarrow{N_i}$ is initialized as (0, −1, 0).

(2) Searching laser-material interaction cells by marching mode.

To trace the multiple reflections of laser rays, the first thing we should do is to find the locations where the rays intersect with the free surface. The main idea of the method applied in this work can be described as a marching mode. To make it easier to understand this process, a 2D schematic diagram is shown in Fig. 4(b). An arbitrary incident ray $\overrightarrow{P_0P_3}$ starts from the point $P_0 = X_i$ with an incident vector $\overrightarrow{N_i}$. Firstly, the P_0 moves to the P_1 by adding an interval vector $\overrightarrow{N}_{\text{interval}}$ along the incidence direction, with an fixed increment Δx in the x-direction. Then we will find the cell center P_1' which is the closest to the P_1 and the P_1 will go on marching along the incidence direction if the volume fraction in the cell centered at P_1' does not meet the criteria: $\varphi_m \leqslant 0.5$ and $\varphi_m > 0$. Finally, this marching mode will be terminated at the P_3 and the P_3' will be targeted as X_i^R the start point of the subsequent reflected ray. For a 3D case, it is emphasized that the largest component of $\overrightarrow{N}_{\text{interval}}$ is fixed at a length of Δx to keep a high marching resolution. For a 3D incidence vector $\overrightarrow{N_i} = (n_x, n_y, n_z)$, the $\overrightarrow{N}_{\text{interval}}$ can be described as:

$$\overrightarrow{N}_{\text{interval}} = \frac{\Delta x}{\max(|n_x|, |n_y|, |n_z|)} \overrightarrow{N} \tag{21}$$

(3) Calculating the reflected rays and cycling.

The reflected ray is calculated based on a geometric optical reflection as shown in Fig. 4(c). The new direction of the reflected ray $\overrightarrow{N_i^R}$ is determined by:

$$\overrightarrow{N_i^R} = \overrightarrow{N_i} - 2(\overrightarrow{N_i} \cdot \overrightarrow{n})\overrightarrow{n} \tag{22}$$

Once the reflection occurs, the variable R_i will be updated by adding 1 to count the reflection number and the power intensity of the reflected ray will be updated as $P_i^R = (1 - A)P_i$, where the laser absorptivity of copper A will be discussed in detail in Section 2.2.4. Meanwhile, the laser heat source in Eq. (8) is calculated by accumulating all the heat sources applied to the reflected grid cells, which can be expressed as:

$$q_{laser} = \sum \frac{AP^i_{laser}}{\Delta x} \varphi_m \tag{23}$$

In this work, the ray-tracing algorithm will be terminated until the rays' power intensity are lower than 1% of corresponding initial level or the reflection paths go beyond the model boundary.

2.2.4. Laser absorption model

The absorption behavior of the laser rays is one of the dominant mechanisms of the laser-material interaction, which is a complex process influenced by several factors, such as the wavelength, material type, incident angle/polarization as well as temperature. In recent literatures, one commonly considered a geometry-dependent Fresnel absorption related to the incident

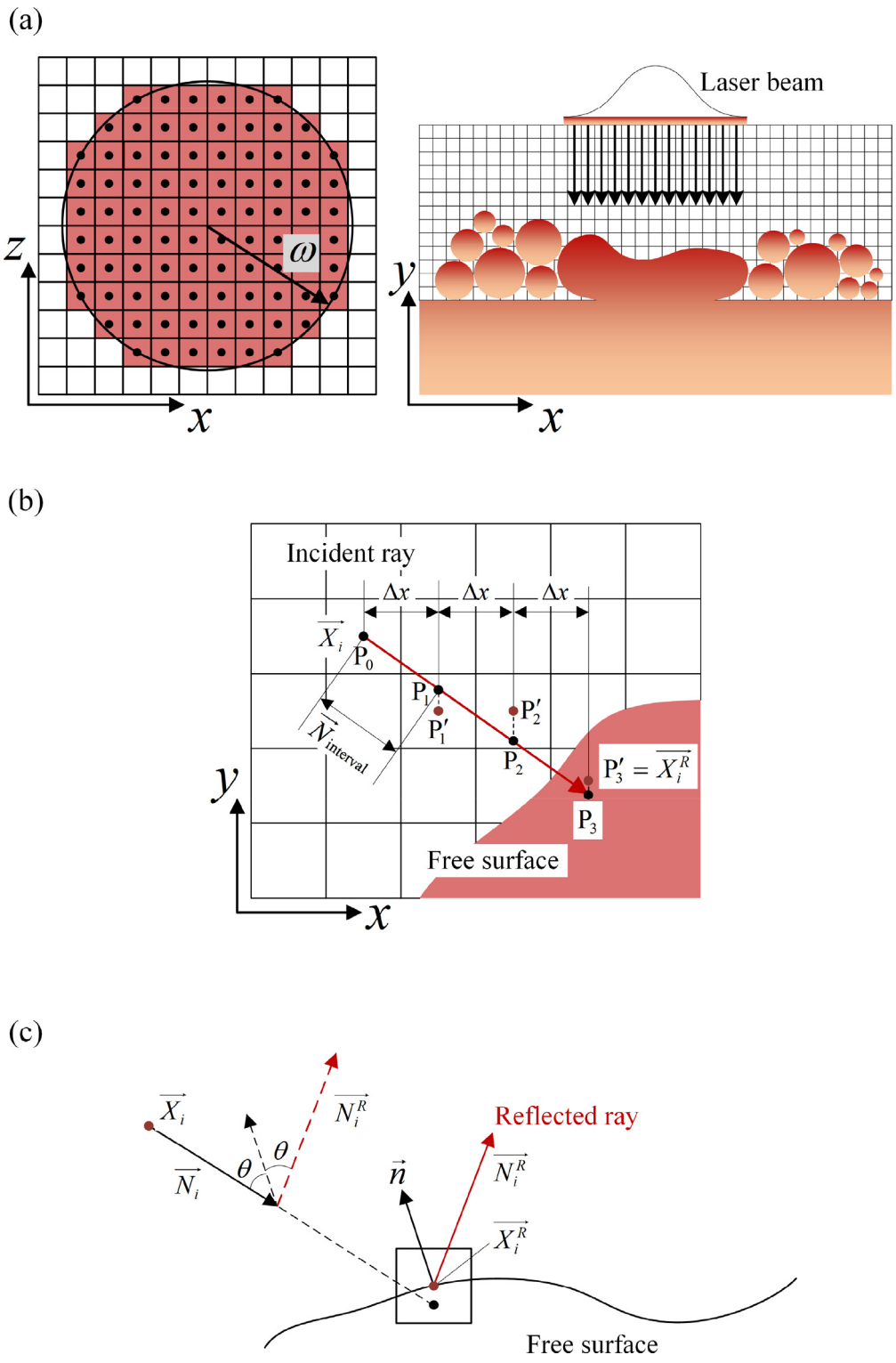

Fig. 4. The schematic diagram of ray-tracing algorithm dependent on grid size.

angle of laser rays, which is characterized as [13,14,25,27,28,41]:

$$A_F = 1 - \frac{1}{2}\left(\left|\frac{\hat{n}^2\cos\theta - (\hat{n}^2 - \sin^2\theta)^{1/2}}{\hat{n}^2\cos\theta + (\hat{n}^2 - \sin^2\theta)^{1/2}}\right|^2 + \left|\frac{\cos\theta - (\hat{n}^2 - \sin^2\theta)^{1/2}}{\cos\theta + (\hat{n}^2 - \sin^2\theta)^{1/2}}\right|^2\right) \quad (24)$$

where the $\hat{n}$ and θ denote the complex index of refraction of the material and the included angle between the incident ray and surface normal vector. In the works by Tang et al. [13] and Bayat et al. [14,27], this model has been successfully used to predict the SLM process of stainless steel 316L with good experimental agreement.

However, there is hardly any research considering the impact of the temperature evolution on the absorption behavior during SLM. In practice, light always interacts with the electrons inside the

metal or the alloy, since light is an electromagnetic wave. The electrons will be accelerated by the electric field and through various collisions with the other constituents of the metal, energy will be transferred to the lattice. As the temperature is elevated, the absorptivity may change, since both the electrons and the lattice atoms in the metal obtain kinetic energy which will affect the collision frequency [12]. Thus, it is in the very nature of things that the present work takes this factor into account to enhance the prediction accuracy of the SLM simulation.

In this study, the Hagan-Ruben relationship is used to estimate the laser absorptivity dependent on the local temperature, which is expressed as [42]:

$$A_H = 4\sqrt{\frac{\pi c_0 \varepsilon_0}{\lambda}\rho_e} \tag{25}$$

where c_0, ε_0, λ denote the light speed in vacuum, vacuum permittivity and laser wavelength, respectively. Since the electrical resistivity ρ_e depends on temperature, the absorptivity A_F can be calculated as a function of temperature. The electrical resistivity can be expressed as a linear function of temperature: $\rho_e = 10^{-8}(a + bT)$, where the coefficients of a and b will vary under different physical states of metal (solid/liquid) as shown in Table 1 [43].

2.3. Model setup and material properties

A computational domain consisted of both fluid (zone 1) and solid (zone 2) domains is created with the global size of $1200 \times 640 \times 400\ \mu m^3$ and the y-direction length divided into 240 μm and 400 μm as shown in Fig. 5. The CFD model is only executed within the fluid domain. The fluid domain is thermally coupled with the solid domain (where only energy conservation equation is solved) using an interface boundary to allow the heat dissipated towards the substrate. The fluid domain is meshed into cubic grids with size of 4 μm and the mesh size in solid domain is set as 8 μm to save the calculation cost.

A laser beam with 80 μm diameter is applied to conduct the single-track simulations with various processing parameters listed in Table 2. The scanning length for each simulated track is set as 1000 μm. The LED level is calculated as: P_{laser}/v_0. Some material properties used in this work are listed in Table 1. The simulation for each case takes about 180–250 h to finish in a workstation with an Intel Core i9-9900K processor.

Table 1
Material properties used in the simulation.

Name of parameters	Value
Density of metal (kg m^{-3})	8927
Density of gas (kg m^{-3})	1.62
Specific heat of metal (J kg^{-1} K^{-1})	380
Specific heat of gas (J kg^{-1} K^{-1})	520.64
Thermal conductivity of solid metal (W m^{-1} K^{-1})	320
Thermal conductivity of liquid metal (W m^{-1} K^{-1})	100
Solidus temperature of Cu-Cr-Zr (K)	1338.7
Liquidus temperature of Cu-Cr-Zr (K)	1355.4
Boiling temperature of Cu-Cr-Zr (K)	2868
Viscosity of metal (Pa s)	0.0043
Surface tension coefficient (N m^{-1})	1.304
Temperature coefficient of surface tension (N m^{-1} K^{-1})	-0.286×10^{-3}
Latent heat of fusion (J kg^{-1})	204,000
Enthalpy change of evaporation (J kg^{-1})	137,170
Electrical resistivity in solid state (Ω m^{-1})	$\rho_e = 10^{-8}(-0.125 + 0.675 \times 10^{-2}T)$
Electrical resistivity in liquid state (Ω m^{-1})	$\rho_e = 10^{-8}(6.2 + 1.02 \times 10^{-2}T)$
Complex index of refraction	$\hat{n} = 0.37863 + 7.0660i$

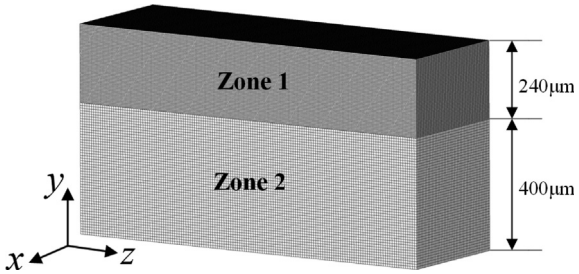

Fig. 5. The meshed computational domain and coordinate system used for simulation.

Table 2
Parameters of SLM single tracks.

Serial number	Laser power (W)	Scanning velocity (m/s)	LED (J/m)	Absorption rule
1	430	0.6	716.7	Fresnel
2	430	0.6	716.7	Hagan-Ruben
3	330	1.2	275	Hagan-Ruben

3. Experimental details

The single-track experiments are conducted by selectively melting a layer of gas-atomized Cu-Cr-Zr powders deposited on an as-built bulk. The recommended processing parameters used for building the bulk are supplied by the SLM system supplier (Suzhou XDM 3D Printing Technology Co., Ltd.) as listed in Table 3, which results in a high relative density of 99.43% compared to the bulk fabricated by forging. The chemical compositions of the Cu-Cr-Zr powders are listed in Table 4 and the size distribution is shown in Fig. 2. The SLM system (XDM 250, XDM Co., ltd, China) works with a fiber laser (IPG Laser GmbH, Germany) with a wavelength of 1064 nm and a maximum output power of 500 W. To observe the melt pool, the as-built bulk with deposited single-tracks is grinded, polished and etched. The etching reagent is a mixed solution of 20 g $FeCl_3$, 5 mL HCl and 100 mL H_2O. The track morphologies in top view and metallographic diagram in cross-section view are observed by a digital microscope (VHX-1000c, Keyence Co., ltd, Japan).

The in-situ laser absorptivity measurements of the Cu-Cr-Zr powders during SLM are carried out based on a direct calorimetric measurement proposed by Trapp et al [26]. Analogous experimental apparatus is built as shown in Fig. 6, with two type K thermocouples weld to the bottom of a thin disc. Two 6 mm single-tracks are processed on the powder layer of the disc with the processing parameters used in the simulations. The powder layer and the thin disc are approximated as a whole with an increase in temperature during SLM. The temperature variation during SLM can be detected by thermocouples and recorded by the temperature detector (JK-8UC, Jinko Electronic Technology Co., Ltd., China).

Table 3
Parameters used for the as-built bulk.

Laser power	Scanning velocity	Hatch space	Powder layer thickness
425 W	0.65 m/s	90 μm	30 μm

Table 4
Chemical compositions (wt.%) of the Cu-Cr-Zr powders.

Cr	Zr	Fe	Si	P	Cu
0.5–1.5	0.05–0.25	<0.05	<0.05	<0.01	Balance

According to the temperature data, the total energy absorbed by the powder-disc system can be calculated. Detailed information about the schematic of calorimetric measurements and calculation can be found in Ref. [26].

4. Results and discussion

4.1. Absorption model comparison and validation

4.1.1. Absorption model comparison

In this work, we firstly compared the simulated melt tracks governed by two different laser absorption rules, namely the familiar Fresnel absorption and the Hagan-Ruben absorption, with other modelling configurations remaining the same. As shown in Fig. 7, the powders fail to melt down in the simulation governed by the Fresnel absorption, and the melting region only exists in the upper part of the powders with small width and depth (42 μm and 11 μm) as observed in the cross-section view. In the situation of the Hagen-Ruben absorption, the formed melt track is obviously continuous, and extends into the substrate which means a sufficient intra-layer adhesion and bonding between the track and substrate, with lager width and depth (135 μm and 94 μm). Additionally, the isometric view of solidified melt track in Fig. 7 demonstrates that the Hagan-Ruben absorption is capable to generate a continuous and integrated single-track, while the Fresnel absorption merely forms a thin and flaked track.

Then, the simulated single-track morphologies are compared with experimental micrography fabricated by same processing parameters. The Fresnel governed track width ranges from 28.4 μm to 57.6 μm with the average value of 47.5 μm, the Hagan-Ruben governed track width ranges from 105.4 μm to 133.2 μm with the average value of 122.4 μm, and the track width from experiment ranges from 91.1 μm to 140.9 μm with the average value of 110.1 μm.

It is obvious that the Hagan-Ruben absorption rule is much more consistent with the actual situation in terms of the track morphology and track width. The huge difference between the two cases can be attributed to the difference in local laser absorptivity based on selected absorption rules, which ultimately impacts the global absorptivity of the powder bed.

As illustrated in Fig. 8, for Hagan-Ruben absorption, the absorptivity that is derived from the variation of the electrical resistivity

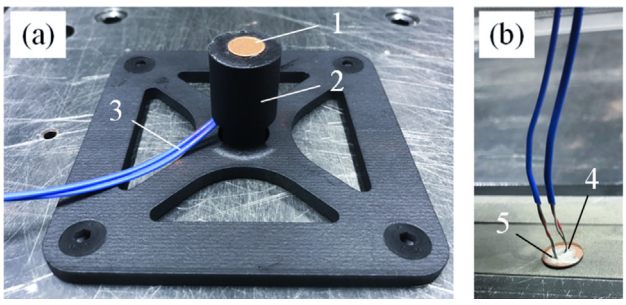

Fig. 6. (a) The view of the custom-built calorimetry apparatus. (b) the Cu-Cr-Zr disc weld with two type K thermocouples. The numbers in the figure refer to (1) the disc containing Cu-Cr-Zr alloy powders, (2) disc holder, (3) thermocouple wires, (4) thermocouple Ⅰ and (5) thermocouple Ⅱ.

ρ_e, has a sharp increase from 10.57% to 15.84% when metal changes from solid to liquid and reaches to the maximum of 21.1% at boiling temperature, while the Fresnel absorptivity is only impacted by the angle of incidence with a maximum value of 5.39%. The global absorptivity is the ratio of the sum of deposited energy from each collision to the total energy of the original laser spot. In this respect, the great difference in the local absorptivity caused by the absorption criterion will directly lead to the change of the global absorptivity.

For the calculated global absorptivity of powder bed, as shown in Fig. 9, we only compared the data from 0 s to 6.23×10^{-4} s, and there is no need to perform a simulation with a full track length of 1000 μm for the Fresnel situation, since the track has reached a steady state. As the melting process reaches a steady state, the calculated global laser absorptivity of Hagan-Ruben ranges from 30.2% to 54.4% with the average value of 40.4%, while that of Fresnel stays from 7.3% to 12.1% with the average value of 9.4%.

Based on the Hagan-Ruben relation, on one hand, the global absorptivity will rise with the temperature elevation. Especially when the solid-liquid phase transition occurs, the gain of the local absorptivity will greatly improve the global absorptivity. On the other hand, the keyhole produced by sufficient energy input will also increase the number of laser reflections [27], thus increasing the global absorptivity. In contrast, the widely-used Fresnel absorption model with a constant complex refractive index fails to completely melt the powders due to the extremely high reflectivity of copper at room temperature. Our key findings on the absorption model at least hint that the familiar Fresnel absorption model has its limitations in the SLM modeling, especially for materials with high reflectivity at room temperature, such as copper and copper alloys, and constructing a temperature-dependent absorption rule based on the Hagan-Ruben relation is a better way to rectify this problem.

To further reflect the advantages of the present laser model, we have also compared the global absorptivity calculated by Gusarov's model [21] defined as Eqs. (26)–(29) with the present work. The detailed parameters used for calculating are listed in Table 5. The global absorptivity calculated by Gusarov's model (33.6%) is obviously lower than the one simulated by the ray-tracing method coupled with Hagen-Ruben absorption (average 40.4%), which may lead to unrealistic lack of fusion. Moreover, since the Gusarov's model only deal with the laser reflection and absorption behavior in the state of powder, the global absorptivity is actually a fixed value in the whole scanning process. However, the real fact is that the laser is absorbed by material in multiple states, namely the powders, molten pool and substrate, and the global absorptivity varies with the time of laser radiation and processing parameters. In this respect, the present study brings better insights into the laser-material interaction.

$$A_{global} = \frac{\rho a}{(4\rho-3)D}\{2(1-\rho^2)e^{-\lambda} - (3+\rho e^{-2\lambda}) \times \{[1+a-\rho(1-a)]e^{2a\lambda} + [1-a-\rho(1+a)]e^{-2a\lambda}\}\} - \frac{3(1-\rho)(1-\rho e^{-2\lambda})}{4\rho-3} \quad (26)$$

$$D = (1-a)[1-a-\rho(1+a)]e^{-2a\lambda} - (1+a)[1+a-\rho(1-a)]e^{2a\lambda} \quad (27)$$

$$\lambda = \frac{3(1-\phi)}{2\phi d_p}L \quad (28)$$

$$a = \sqrt{1-\rho} \quad (29)$$

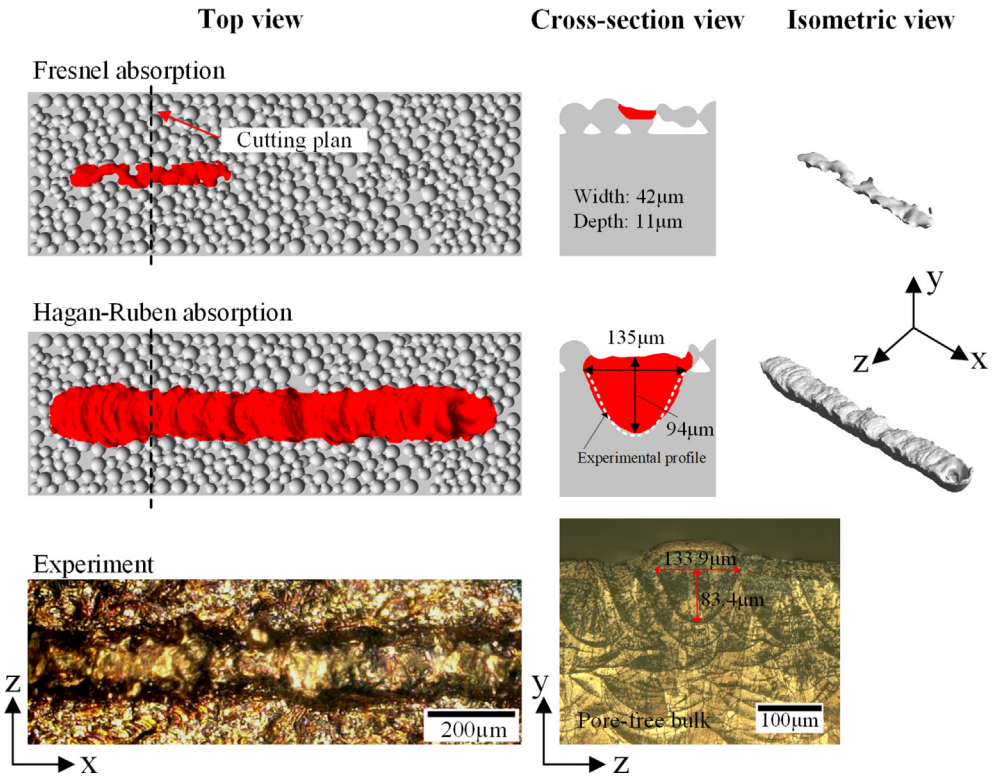

Fig. 7. The simulated single-track morphologies ruled by different absorption rules: Fresnel (top) and Hagan-Ruben (middle), compared with the experimental micrography (bottom) under the same processing parameters (P = 430 W and V = 0.6 m/s). The red region indicates the solidified region after the laser beam moves away. Each column of subfigures corresponds to the top view of track morphologies, cross-section view at the cutting plan, and the isometric view of solidified melt tracks. (For interpretation of the references to colour in this figure legend, the reader is referred to the web version of this article.)

4.1.2. In-situ absorptivity measurements and validation

Two single-tracks are processed on the Cu-Cr-Zr powders of the calorimetry apparatus and the temperature curves obtained by the two thermocouples are presented in Fig. 10. According to the Trapp's work [26], the temperature curves detected by thermocouple Ⅰ and Ⅱ will tend to overlap after a period of cooling time, and an exponential function ($T(t) = T_1 \exp(-t/t_m) + T_0$ with t_m being a constant) is fitted to temperature data in the overlap range. The effective temperature T_1 corresponding to the time when the tracks are processed can be extrapolated from the fitted function. With known the temperature increase of the powder-disc system, the effective absorptivity in SLM can be calculated by Eq. (30)

$$A_{eff} = \frac{\int_{T_0}^{T_1} mC_p dT}{Pl/v} \tag{30}$$

where m, C_p, P, l and v indicate the mass of the powder-disc system, the specific heat of Cu-Cr-Zr, the laser power, the single-track length and the scanning velocity.

The calculated values of the effective laser absorptivity are 40.24% (P = 430 W and v = 0.6 m/s) and 27.04% (P = 330 W and v = 1.2 m/s) respectively. The calculated values of the laser absorptivity from calorimetric measurements are listed in Table 6, which shows good agreement with the simulation results. The accuracy of thermocouples, estimated mass of powder-disc system, heat loss

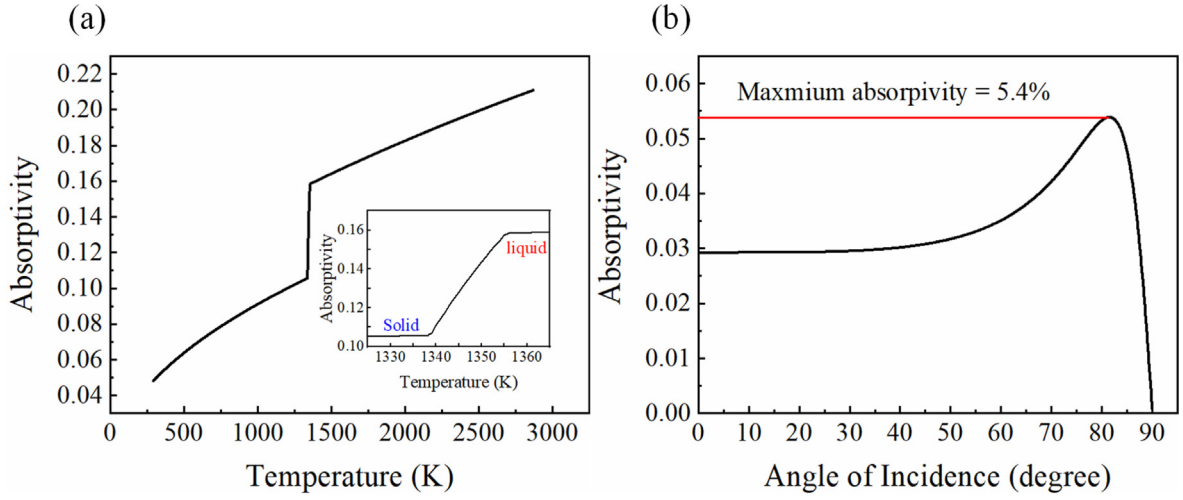

Fig. 8. (a) The local absorptivity versus temperature for Hagan-Ruben absorption, and (b) the local absorptivity versus the incident angle of laser ray for Fresnel absorption.

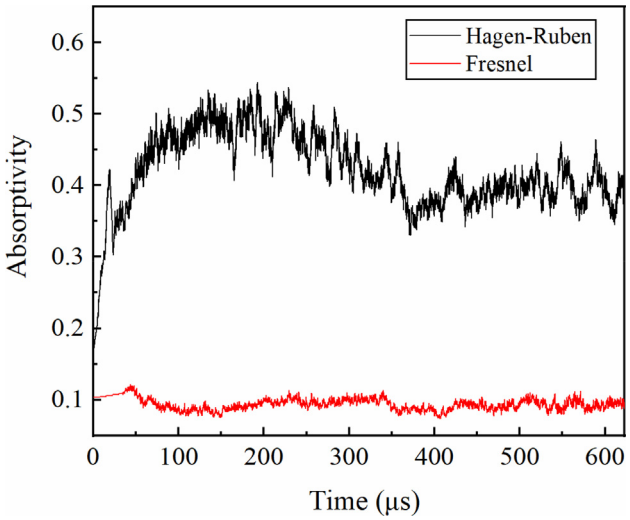

Fig. 9. The global laser absorptivity of powder bed versus time for two different absorption rules.

Table 5
Parameters used to calculate the global absorptivity for copper alloy by Gusarov's model.

Name of parameters	Symbol	value
Laser reflectivity of dense solid	ρ	0.96
Layer thickness (μm)	L	55
Powder porosity	ϕ	0.5
Mean diameter of powders (μm)	d_p	32

from the disc holder and thermocouple wires, etc., may lead to the experimental error [26], but the maximum error between experiment and simulation is lower than 2%, which is supposed to be acceptable.

4.2. Laser reflection mechanisms during the evolution of the melt pool

The reflection mechanisms during SLM are closely related to the complex fluid dynamics of molten materials, which is a result of the combination of various driving forces and heat transfer. Based on the flow kinetics and ray trajectories observed in the simulations, this work provides an insight into the underlying mechanisms of laser reflections during the evolution of melt pool.

As a basic building unit, a sing-track of good quality is the foundation of a defect free final product, which is closely related to the processing parameters used in SLM. Many studies have shown that low linear energy density (LED) can lead to the single-track discontinuity as well as poor bonding quality with previously processed layers, while high LED level causes overheated region that ultimately results in keyhole-induced voids. However, the occasion of keyhole-induced voids is not studied in this study. On the one hand, Bayat et al. [27] have done detailed research on the laser reflection behavior as a keyhole is formed in SLM. On the other hand, the high thermal conductivity and reflectivity make it difficult for copper alloy to produce a large depth of thermal penetration and form keyhole-induced bubbles. According to the metallographic diagram of corrosion in Fig. 7, no typical spherical keyhole bubbles are observed at a relatively high LED parameter (P = 430 W and V = 0.6 m/s). In addition, when we used a higher LED (P = 480 W and V = 0.3 m/s) for 30 min processing, the laser galvanometer system sent out an alarm message. Thus, too high LED level may not only lead to potential keyhole bubbles, but also damage the SLM processing system of copper or copper alloys [8]. In this respect, this section only discusses the mechanisms of laser reflection for two cases (i.e., the continuous and discontinuous tracks) respectively under different LED levels.

4.2.1. Reflection and flow behaviors in the case of continuous track

As a relatively high LED (P = 430 W and V = 0.6 m/s) is applied, a continuous melt track is acquired in the simulation with the Hagan-Ruben absorption as shown in Fig. 7. It can be obviously seen from Section 4.1 that the global absorptivity varies dynamically with time. Fig. 11 presents the entire process of the oscillating global absorptivity for the 1 mm long single-track, with the same processing parameters as used in Section 4.1. The oscillating curve of global absorptivity is analyzed by polynomial regression, with the fitting equation expressed as:

$$y = 0.245 + 4.28e^{-3}x - 2.6e^{-5}x^2 + 6.88e^{-8}x^3 - 9.54e^{-11}x^4 + 7.19e^{-14}x^5 - 2.8e^{-17}x^6 + 4.4e^{-21}x^7 + \varepsilon \quad (31)$$

From the perspective of the general trend for the whole track formation, the evolution of global absorptivity can be divided into three stage as observed in the regression curve. To identify the

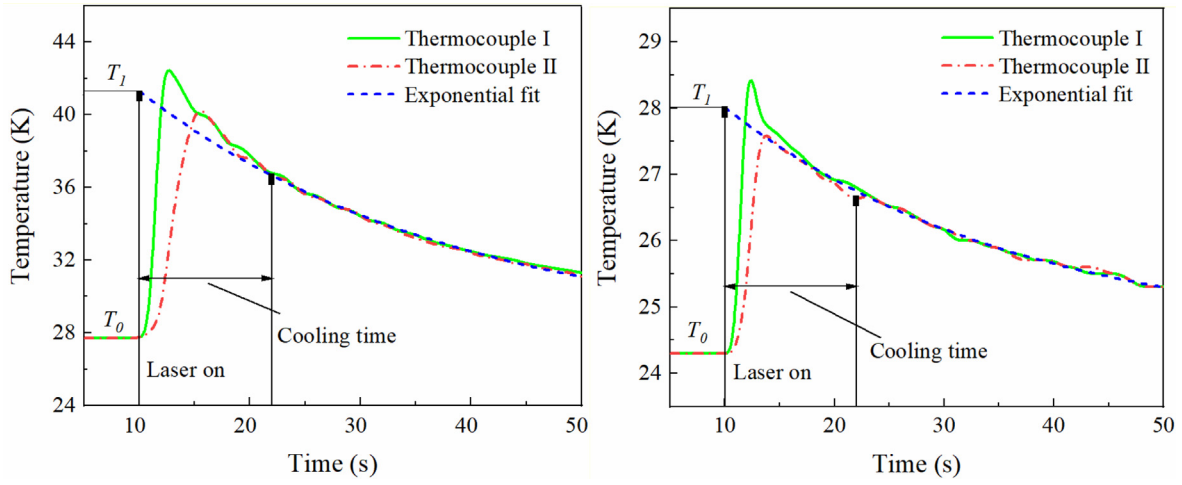

Fig. 10. Temperature curves versus time obtained by thermocouples under different processing parameters (left: laser power = 430 W and scanning velocity = 0.6 m/s; right: laser power = 330 W and scanning velocity = 1.2 m/s).

Table 6
The values of laser absorptivity from experiments and simulation with different processing parameters.

Laser parameters	Effective laser absorptivity A_{eff} by calorimetric measurements	Global absorptivity A_{global} simulated by the Hagan-Ruben relation
P = 430 W, v = 0.6 m/s	40.24%	40.4%
P = 330 W, v = 1.2 m/s	27.04%	25.1%

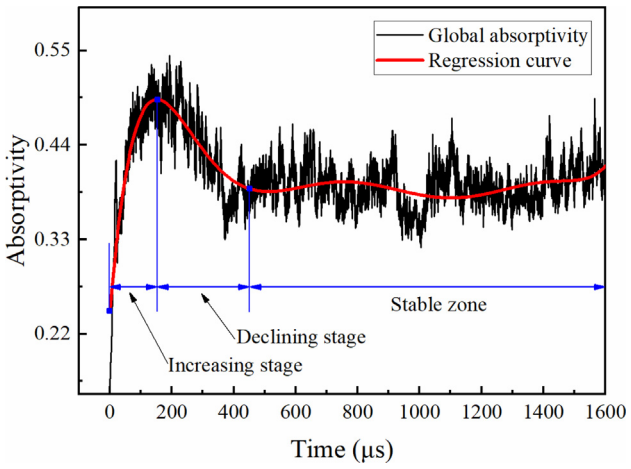

Fig. 11. The black curve indicates the global absorptivity versus time for the whore process of SLM single-track, under the processing parameters (laser power P = 430 W, scanning velocity V = 0.6 m/s). The red curve is the fitting curve of global absorptivity by polynomial regression. (For interpretation of the references to colour in this figure legend, the reader is referred to the web version of this article.)

characteristics of these three stages, several time snapshots of the melt flow with the reflected ray vectors on the free surface are also illustrated in Fig. 12.

In the first increasing stage, the powders are heated by the laser beam with the global absorptivity continuously rising from 0 μs to 152 μs. According to Fig. 12(a)-(c), multiple reflection and absorption of laser rays firstly occur in the solid powders, with a relatively low absorptivity of 16.2% at 4.4 μs. Then the free surface of generated melt pool is pushed downward with a depression region formed at 55 μs, which is directly derived from the vapor recoil pressure as discussed in many literatures. On the one hand, the increasing temperature within the melt pool undoubtedly enhance the global absorptivity according to the Hagan-Ruben relation. On the other hand, the formed depression region allows more ray reflections, thus elevating the global absorptivity to a higher level of 41.7%. Under continuous heating, the absorptivity reaches to the peak level of 50.1% at 152 μs with the depression region extending to a deeper depth. Comparing to the moment of 55 μs, the calculated surface area of melt pool (MPA) at 152 μs is obviously higher than the former, which implies that the expanded curved surface within the depression region will become a better reflector for laser reflections, thus boosting the absorptivity. Additionally, the average temperature on the melt pool surface (MPAT) also increases, which thus contributes to the increase in absorptivity.

In the second stage, the global absorptivity has a downward trend. As shown in Fig. 12(d), when the SLM process lasts for 472 μs, a metallurgical solidified region has been formed behind the melt pool, with a relatively burly tail end observed in the beginning of the sing-track and a shrinkage of melt track right in front of the tail end. This can be explained by the fact that the solidified region can be considered as a kind of better conductor than loose powders. At the beginning of the single-track scanning, the heat dissipation environment around the melt pool is poor since the gas phase between the loose powders hinders the heat conduction process, thus resulting in more heat accumulation. The formation of solidified region at 472 μs will improve the heat conduction condition, which thus leads to the decrease of heat accumulation and size of the melt pool. This is also reflected in the decrease of MPA and MPAT through comparing Fig. 12(c) and (d). Generally, the formation solidified region behind the melt pool plays a vital role in the declining of global absorptivity, since the decrease of MPA means less reflections on the melt pool surface and the reduction of MPAT denotes the decrease of local absorptivity.

In the third stage, since there has reached a balance between the heat dissipation and laser energy input, the shape and size of the melt pool will not change much as shown in Fig. 12(d) and (e). We also find that the values of MPA and MPTA at 729 μs compared to 472 μs decrease and increase slightly, respectively, while the values of global absorptivity at tow moments are almost the same.

In the view of a smaller time scale, it is important to highlight that the absorptivity oscillates near the regression curve as observed in Fig. 11. This may be caused by the random distribution of powder particles, resulting in a change in the shape and flow state of the molten pool at every moment of the scanning process. The variation of the free surface of laser interacting with metal material will directly lead to the change of the reflection trajectory, which in turn affects the energy input of the melt pool and leads to the geometry change of the melt pool. From this standpoint, the dynamic oscillation of global absorptivity is taken for granted and similar calculation results can be also found in researches by Tang et al. [13] and Bayat et al. [27].

4.2.2. Reflection and flow behaviors when the balling effect occurs

When the processing parameters are set as P = 330 W and V = 1.2 m/s with a relatively low LED level, the balling effect is observed in both experimental and simulated results as shown in Fig. 13. The detailed formation process of the balling effect is depicted in Fig. 14. At 11 μs to 51 μs, the powder particles that are initially in contact with each other are heated and merge together to form a melt pool at 51 μs. For this period, the global absorptivity continues to increase due to the temperature elevation on the laser-material acting surface. At 71 μs, the previously formed melt pool evolves into an isolated island (ball) as shown in Fig. 14(c1) and (c2), since the unmelted substrate leads to a pool wettability and the melt pool prefers to cluster to minimize the surface energy rather than spread on the substrate [18]. Meanwhile, the formation of isolated ball leaves part of the substrate exposed to the laser spot. This causes massive laser rays to radiate on the flat unmelted substrate and reflect vertically into the environment, consequently leading to a decline in global absorptivity from 26.2% at 51 μs to 21.1% at 71 μs. From 71 μs to 101 μs, the newly generated floating cluster 2 is dragged into the previously formed floating cluster 1 to form a lager merged cluster. This also leaves part of the substrate exposed to the laser beam, while the global absorptivity remains at about the same level as at 71 μs. From 121 μs to 191 μs, since most of the area covered under the laser spot is heated to liquid, the global absorptivity continues to rise to 25.1% at 191 μs. At 221 μs, analogous balling effect occurs driven by the surface tension, and the consequent exposed substrate leads to a decrease in global absorptivity from 25.1% to 24.6%. At 231 μs, the spheroidization of the melt pool becomes more pronounced, while the center of the laser beam moves to the exposed substrate as shown in Fig. 14(h1) and (h2).

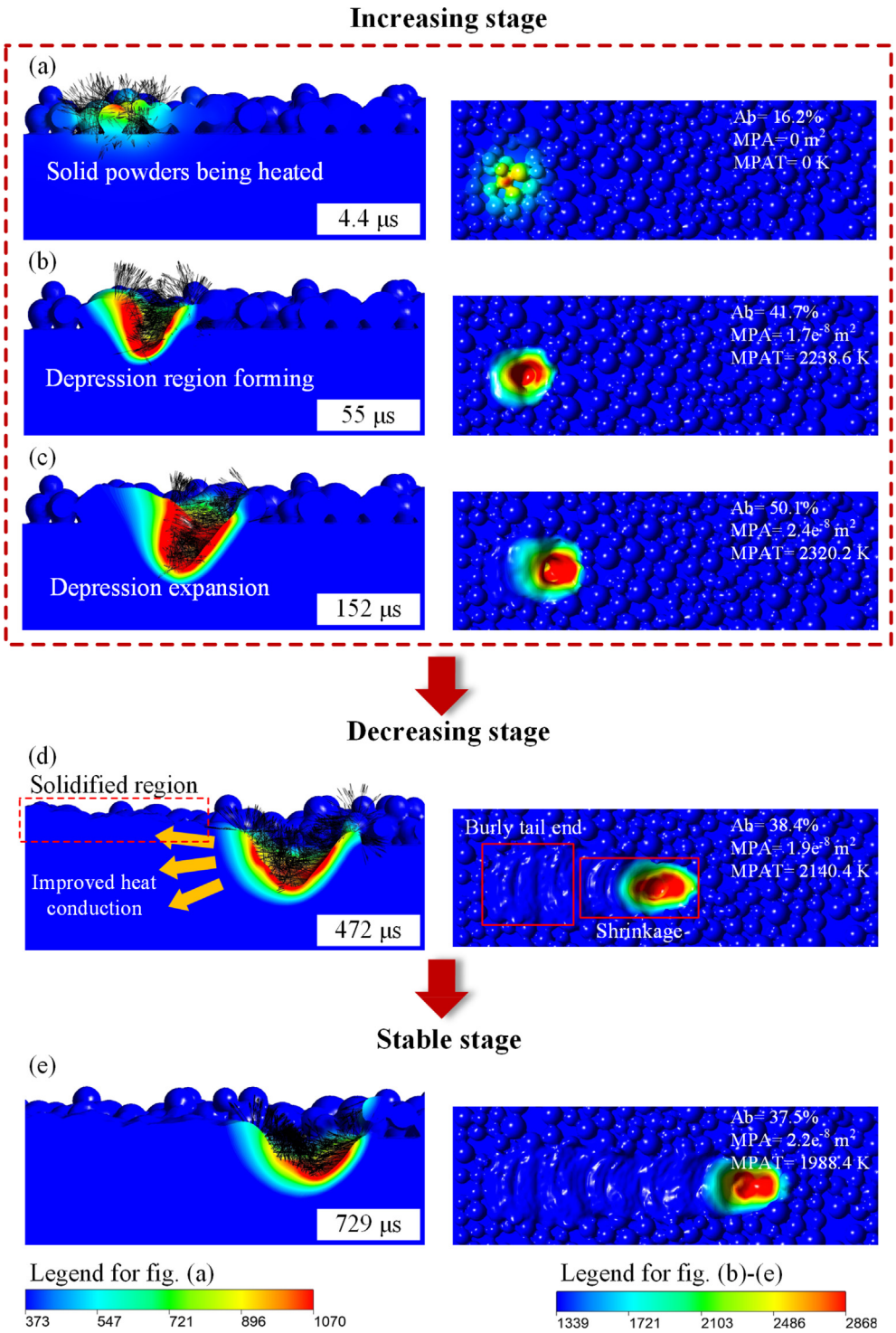

Fig. 12. Time snapshots showing the evolution of the free surface temperature and reflected ray vectors. Ab, MPA and MPAT stand for the global absorptivity, the area of melt pool surface and the average temperature on the melt pool surface, respectively.

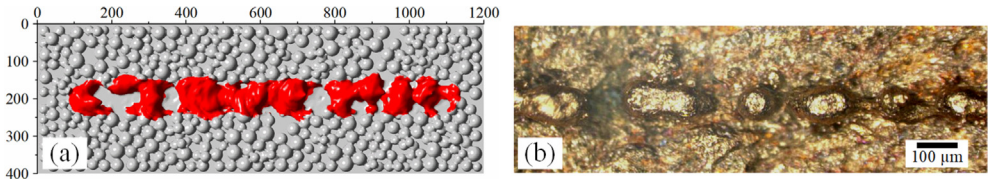

Fig. 13. The simulated (a) and experimental (b) track morphology under a low LED level (laser power P = 330 W and scanning velocity V = 1.2 m/s). The solidified region in the simulation is highlighted in red. (For interpretation of the references to colour in this figure legend, the reader is referred to the web version of this article.)

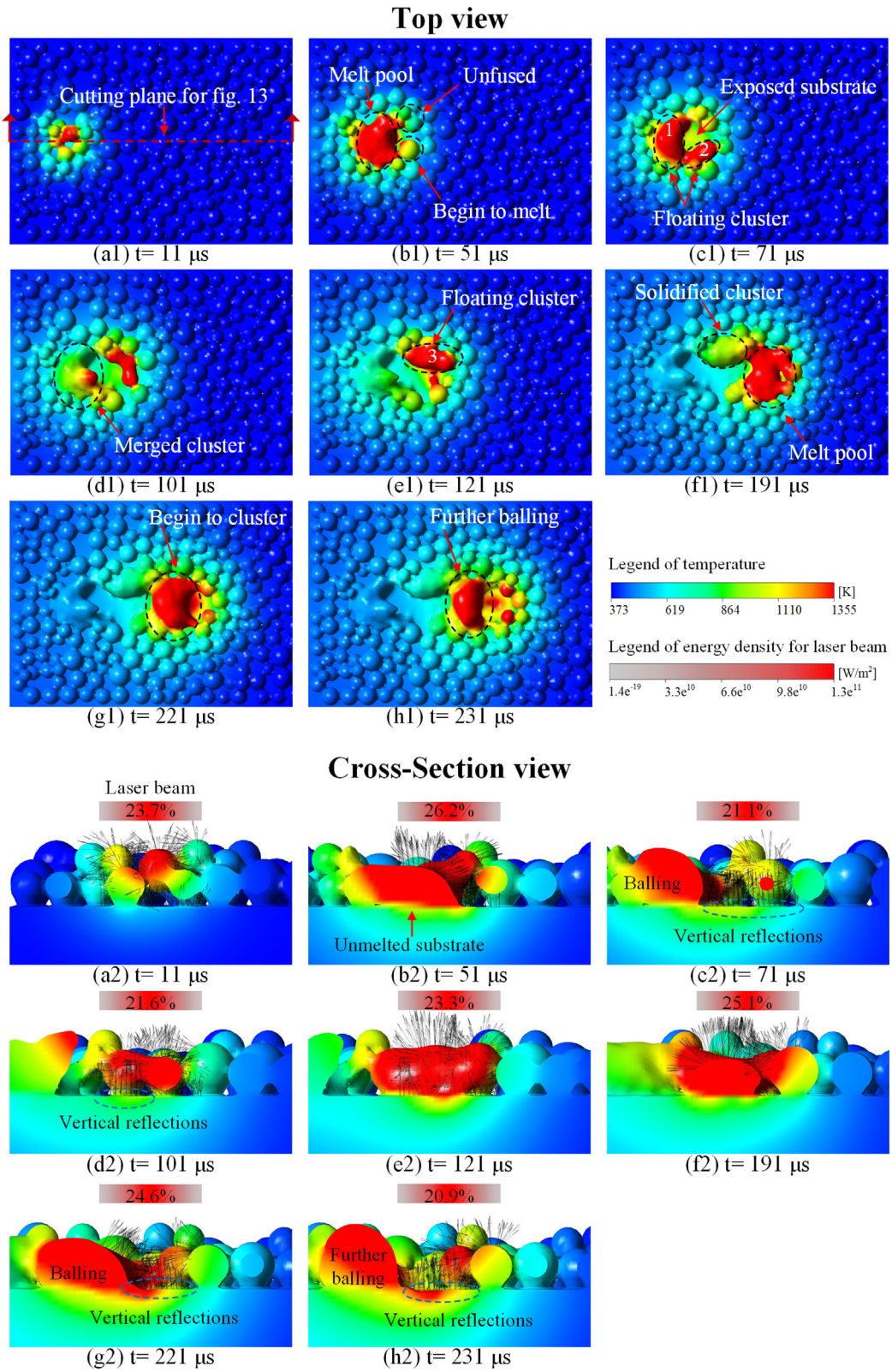

Fig. 14. Time snapshots of the melt pool evolution when the balling effect occurs. The value of global absorptivity for each time is labeled in the laser beam.

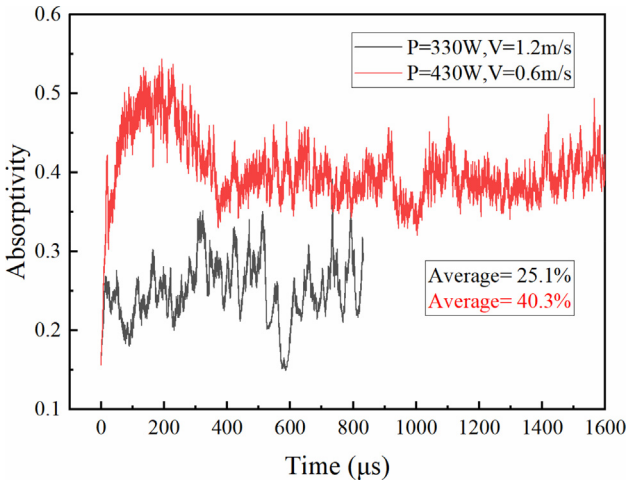

Fig. 15. The global absorptivity for high and low LED levels.

Consequently, the global absorptivity drops sharply to 20.9% at 231 μs due to massive vertical reflections.

4.2.3. The comparison of global absorptivity between continuous and discontinuous tracks

Fig. 15 shows the variation of global absorptivity with time during the single-track scanning, under different LED levels. As aforementioned, the global absorptivity at high LED will go through the process of climbing and decreasing in the initial stage, and finally remain at a relatively stable level. However, the global absorptivity at low LED shows more intense oscillation than that at high LED during the whole scanning. The average absorptivity at low LED is only kept at 25.1%, while that at high LED is 40.3%. The intense oscillation is closely related to the balling process of the melt pool induced by insufficient energy input. Based on previous analysis, the emerging isolated balls and exposed surface of the substrate will lead to a severe decrease in global absorptivity as shown in Fig. 14(b2-c2) and (g2-h2), while a higher absorptivity will be obtained as the laser spot is covered on the surface of liquid metal. Thus, as the balling process evolves, the low-LED absorptivity is extremely unstable. On the contrary, the geometry and size of the melt pool at high LED is much more stable as discussed in Section 4.2.1, and slight oscillation of absorptivity is mainly ascribed to the random distribution of powder particles. Obviously, the global absorptivity is affected by the processing parameters due to the difference in the temperature and geometry of the reflecting surface. Moreover, the global absorptivity under higher LED level is generally greater than that at low LED, which is also validated by the experiments via the direct calorimetric measurements of the effective absorptivity in the work of Trapp et al. [26].

5. Conclusion

With a high-fidelity CFD model developed for the single-track simulation, this work has a comprehensive study on the laser reflection behavior in SLM of copper alloy. Several conclusions can be summarized as follows:

(1) This work provides a modified CFD model to more accurately predict the SLM process of copper alloy, and reveals the underlying mechanisms of laser reflections in two cases: continuous and discontinuous single-tracks. Other influencing factors like the hatch space, the thickness of the powder layer, etc. should be discussed in future work.

(2) The widely-used Fresnel absorption rule has its limitation in the SLM modeling for materials with high reflectivity, while the Hagan-Ruben relation has a good performance in the simulation to form a continuous single-track.

(3) For a continuous single-track, the global absorptivity generally undergoes three stages: increasing, declining and keeping stable, which is related to the heat conduction environment during the scanning process. In addition, the evolution of the melt pool and the random distribution of powder particles will lead to dynamic oscillation of the global absorptivity.

(4) As the balling effect occurs, the global absorptivity has a relative low level and fluctuates intensely during entire scanning process. Such intense oscillation is due to the unstable melt pool derived from the poor wettability of the melt pool on the substrate. More specifically, the vertical reflections on the emerging exposed substrate greatly contribute to the reduction of global absorptivity and lead to the intense oscillation.

(5) With the ray-tracing method and Hagan-Ruben absorption rule introduced in the simulation, the global absorptivity is found to be varied with processing parameters. It is worth noting that a high LED level not only improves the wettability to form a relatively stable melt pool, but also increases the global absorptivity due to the ray-entrapment in the depression region. It is recommended that an appropriate LED should be adopted to avoid the balling effect that consequently leads to the instability and reduction of global absorptivity.

Declaration of Competing Interest

The authors declare that they have no known competing financial interests or personal relationships that could have appeared to influence the work reported in this paper.

Acknowledgements

The authors gratefully acknowledge the financial support by Natural Science Foundation of Chongqing, China [grant number. cstc2020jcyj-zdxmX0021]; the Fundamental Research Funds for the Central Universities [grant number. 0209005202109]; and Project supported by graduate research and innovation foundation of Chongqing, China [grant number. GYB20011].

References

[1] W.E. King, A.T. Anderson, R.M. Ferencz, N.E. Hodge, C. Kamath, S.A. Khairallah, A.M. Rubenchik, Laser powder bed fusion additive manufacturing of metals; physics, computational, and materials challenges, Appl. Phys. Rev. 2 (4) (2015).
[2] N. Guo, M.C. Leu, Additive manufacturing: technology, applications and research needs, Front. Mech. Eng. 8 (3) (2013) 215–243.
[3] S. Zhang, H. Zhu, Z. Hu, X. Zeng, F. Zhong, Selective Laser Melting of Cu 10Zn alloy powder using high laser power, Powder Technol. 342 (2019) 613–620.
[4] J. Tian, W. Zhu, Q. Wei, S. Wen, S. Li, B. Song, Y. Shi, Process optimization, microstructures and mechanical properties of a Cu-based shape memory alloy fabricated by selective laser melting, J. Alloy. Compd. 785 (2019) 754–764.
[5] Z. Tan, X. Zhang, Z. Zhou, Z. Zhou, Y. Yang, X. Guo, Z. Wang, X. Wu, G. Wang, D. He, Thermal effect on the microstructure of the lattice structure Cu-10Sn alloy fabricated through selective laser melting, J. Alloy. Compd. 787 (2019) 903–908.
[6] P.R. Gradl, C.S. Protz, K. Cooper, D. Ellis, L.J. Evans, C. Garcia, GRCop-42 Development and Hot-fire Testing Using Additive Manufacturing Powder Bed Fusion for Channel-cooled Combustion Chambers, AIAA Propulsion and Energy 2019 Forum, 2019.
[7] T.Q. Tran, A. Chinnappan, J.K.Y. Lee, N.H. Loc, L.T. Tran, G. Wang, V.V. Kumar, W. A.D.M. Jayathilaka, D. Ji, M. Doddamani, S. Ramakrishna, 3D printing of highly pure copper, Metals 9 (7) (2019).

[8] S.D. Jadhav, S. Dadbakhsh, L. Goossens, J.P. Kruth, J. Van Humbeeck, K. Vanmeensel, Influence of selective laser melting process parameters on texture evolution in pure copper, J. Mater. Process. Technol. 270 (2019) 47–58.
[9] Z. Mao, D.Z. Zhang, J. Jiang, G. Fu, P. Zhang, Processing optimisation, mechanical properties and microstructural evolution during selective laser melting of Cu-15Sn high-tin bronze, Mater. Sci. Eng., A 721 (2018) 125–134.
[10] D. Zhang, Z. Liu, C. Chua, Investigation on forming process of copper alloys via Selective Laser Melting, High Value Manufacturing: advanced Research in Virtual and Rapid Prototyping: Proceedings of the 6th International Conference on Advanced Research in Virtual and Rapid Prototyping, Leiria, Portugal, 2013, p. 285.
[11] T. Gustmann, H. Schwab, U. Kühn, S. Pauly, Selective laser remelting of an additively manufactured Cu-Al-Ni-Mn shape-memory alloy, Mater. Des. 153 (2018) 129–138.
[12] D. Bergström, The absorptance of metallic alloys to Nd:YAG and Nd:YLF laser light, Licentiate thesis / Luleå University of Technology, Luleå tekniska universitet, Luleå, 2005, p. 8.
[13] C. Tang, K.Q. Le, C.H. Wong, Physics of humping formation in laser powder bed fusion, Int. J. Heat Mass Transf. 149 (2020).
[14] M. Bayat, S. Mohanty, J.H. Hattel, Multiphysics modelling of lack-of-fusion voids formation and evolution in IN718 made by multi-track/multi-layer L-PBF, Int. J. Heat Mass Transf. 139 (2019) 95–114.
[15] C. Panwisawas, C.L. Qiu, Y. Sovani, J.W. Brooks, M.M. Attallah, H.C. Basoalto, On the role of thermal fluid dynamics into the evolution of porosity during selective laser melting, Scr. Mater. 105 (2015) 14–17.
[16] S.A. Khairallah, A.T. Anderson, A. Rubenchik, W.E. King, Laser powder-bed fusion additive manufacturing: physics of complex melt flow and formation mechanisms of pores, spatter, and denudation zones, Acta Mater. 108 (2016) 36–45.
[17] C. Qiu, C. Panwisawas, M. Ward, H.C. Basoalto, J.W. Brooks, M.M. Attallah, On the role of melt flow into the surface structure and porosity development during selective laser melting, Acta Mater. 96 (2015) 72–79.
[18] W. Yan, W. Ge, Y. Qian, S. Lin, B. Zhou, W.K. Liu, F. Lin, G.J. Wagner, Multi-physics modeling of single/multiple-track defect mechanisms in electron beam selective melting, Acta Mater. 134 (2017) 324–333.
[19] C. Tang, J.L. Tan, C.H. Wong, A numerical investigation on the physical mechanisms of single track defects in selective laser melting, Int. J. Heat Mass Transf. 126 (2018) 957–968.
[20] Y.S. Lee, W. Zhang, Modeling of heat transfer, fluid flow and solidification microstructure of nickel-base superalloy fabricated by laser powder bed fusion, Addit. Manuf. 12 (2016) 178–188.
[21] A.V. Gusarov, I. Yadroitsev, P. Bertrand, I.J.J.o.H.T. Smurov, Model of Radiation and Heat Transfer in Laser-Powder Interaction Zone at Selective Laser Melting, Journal of Heat Transfer 131(7) (2009) 70-79.
[22] M. Xia, D. Gu, G. Yu, D. Dai, H. Chen, Q. Shi, Influence of hatch spacing on heat and mass transfer, thermodynamics and laser processability during additive manufacturing of Inconel 718 alloy, Int. J. Mach. Tools Manuf 109 (2016) 147–157.
[23] G.X. Xu, C.S. Wu, G.L. Qin, X.Y. Wang, S.Y. Lin, Adaptive volumetric heat source models for laser beam and laser + pulsed GMAW hybrid welding processes, Int. J. Adv. Manuf. Technol. 57 (1–4) (2011) 245–255.
[24] G. Fu, D. Zhang, A. He, Z. Mao, K. Zhang, Finite element analysis of interaction of laser beam with material in laser metal powder bed fusion process, Materials 11 (5) (2018).
[25] C.D. Boley, S.A. Khairallah, A.M. Rubenchik, Calculation of laser absorption by metal powders in additive manufacturing, Appl. Opt. 54 (9) (2015) 2477–2482.
[26] J. Trapp, A.M. Rubenchik, G. Guss, M.J. Matthews, In situ absorptivity measurements of metallic powders during laser powder-bed fusion additive manufacturing, Appl. Mater. Today 9 (2017) 341–349.
[27] M. Bayat, A. Thanki, S. Mohanty, A. Witvrouw, S. Yang, J. Thorborg, N.S. Tiedje, J.H. Hattel, Keyhole-induced porosities in Laser-based Powder Bed Fusion (L-PBF) of Ti6Al4V: High-fidelity modelling and experimental validation, Addit. Manuf. 30 (2019).
[28] B. Liu, G. Fang, L. Lei, W. Liu, A new ray tracing heat source model for mesoscale CFD simulation of selective laser melting (SLM), Appl. Math. Model. 79 (2020) 506–520.
[29] X. Xu, M. Schmid, S. Zehnder, P. Schwaller, B. Neuenschwander, J. Zürcher, U. Hunziker, G. Hennig, Y. Nakata, S.W. Roth, Measuring the complex refractive index of metals in the solid and liquid state and its influence on the laser machining, Laser Applications in Microelectronic and Optoelectronic Manufacturing (LAMOM) XVIII, 2013.
[30] M. Schmid, S. Zehnder, P. Schwaller, B. Neuenschwander, M. Held, U. Hunziker, J. Zürcher, Measuring optical properties on rough and liquid metal surfaces, ALT Proceedings 1 (2012).
[31] K. Ujihara, Reflectivity of metals at high temperatures, J. Appl. Phys. 43 (5) (1972) 2376–2383.
[32] Z. Ma, K. Zhang, Z. Ren, D.Z. Zhang, G. Tao, H. Xu, Selective laser melting of Cu–Cr–Zr copper alloy: parameter optimization, microstructure and mechanical properties, J. Alloy. Compd. 828 (2020).
[33] Y. Zhao, Y. Koizumi, K. Aoyagi, K. Yamanaka, A. Chiba, Characterization of powder bed generation in electron beam additive manufacturing by discrete element method (DEM), Mater. Today:. Proc. 4 (11) (2017) 11437–11440.
[34] D. Solutions, EDEM 2.6 theory reference guide, Edinburgh, United Kingdom, 2014.
[35] C.W. Hirt, B.D. Nichols, Volume of fluid (VOF) method for the dynamics of free boundaries, J. Comput. Phys. 39 (1) (1981) 201–225.
[36] Y. Zhang, J. Zhang, Modeling of solidification microstructure evolution in laser powder bed fusion fabricated 316L stainless steel using combined computational fluid dynamics and cellular automata, Addit. Manuf. 28 (2019) 750–765.
[37] S.A. Khairallah, A. Anderson, Mesoscopic simulation model of selective laser melting of stainless steel powder, J. Mater. Process. Technol. 214 (11) (2014) 2627–2636.
[38] Z.S. Saldi, Marangoni driven free surface flows in liquid weld pools, Multi Scale Physics, Delft University of Technology, 2012.
[39] J.-H. Cho, D.F. Farson, J.O. Milewski, K.J. Hollis, Weld pool flows during initial stages of keyhole formation in laser welding, J. Phys. D Appl. Phys. 42 (17) (2009).
[40] D. Zhang, P. Zhang, Z. Liu, Z. Feng, C. Wang, Y. Guo, Thermofluid field of molten pool and its effects during selective laser melting (SLM) of Inconel 718 alloy, Addit. Manuf. 21 (2018) 567–578.
[41] J.-H. Cho, S.-J. Na, Implementation of real-time multiple reflection and Fresnel absorption of laser beam in keyhole, J. Phys. D Appl. Phys. 39 (24) (2006) 5372–5378.
[42] R.E. Hummel, Electronic Properties of Materials, forth ed., Springer, New York, 2011.
[43] J. Xie, A. Kar, J.A. Rothenflue, W.P. Latham, Temperature-dependent absorptivity and cutting capability of CO2, Nd: YAG and chemical oxygen–iodine lasers, J. Laser Appl. 9 (2) (1997) 77–85.